

Efficient Image-to-Image Schrödinger Bridge for CT Field of View Extension

Zhenhao Li, Long Yang, Xiaojie Yin, Haijun Yu, Jiazhou Wang, Hongbin Han, Weigang Hu, Yixing Huang

Abstract—Computed tomography (CT) is a cornerstone imaging modality for non-invasive, high-resolution visualization of internal anatomical structures. However, when the scanned object exceeds the scanner’s field of view (FOV), projection data are truncated, resulting in incomplete reconstructions and pronounced artifacts near FOV boundaries. Conventional reconstruction algorithms struggle to recover accurate anatomy from such data, limiting clinical reliability. Deep learning approaches have been explored for FOV extension, with diffusion generative models representing the latest advances in image synthesis. Yet, conventional diffusion models are computationally demanding and slow at inference due to their iterative sampling process. To address these limitations, we propose an efficient CT FOV extension framework based on the image-to-image Schrödinger Bridge (I^2SB) diffusion model. Unlike traditional diffusion models that synthesize images from pure Gaussian noise, I^2SB learns a direct stochastic mapping between paired limited-FOV and extended-FOV images. This direct correspondence yields a more interpretable and traceable generative process, enhancing anatomical consistency and structural fidelity in reconstructions. I^2SB achieves superior quantitative performance, with root-mean-square error (RMSE) values of 49.8 HU on simulated noisy data and 152.0 HU on real data—outperforming state-of-the-art diffusion models such as conditional denoising diffusion probabilistic models (cDDPM) and patch-based diffusion methods. Moreover, its one-step inference enables reconstruction in just 0.19 s per 2D slice, representing over a 700-fold speedup compared to cDDPM (135 s) and surpassing diffusionGAN (0.58 s), the second fastest. This combination of accuracy and efficiency makes I^2SB highly suitable for real-time or clinical deployment.

Index Terms—Computed tomography, field-of-view, Schrödinger bridge, diffusion models, data truncation, deep learning

I. INTRODUCTION

COMPUTED tomography (CT) enables high-resolution, non-invasive imaging of internal structures, with widespread applications in the medical fields [1]. In a typical CT scanning scenario, a detector rotates around an imaged object to acquire projection data for reconstruction. However, in many clinical applications such as radiation therapy [2], [3], spine surgery [4], body composition analysis [5], [6], and brain region-of-interest (ROI) imaging [7], collected projection data may suffer from the data truncation problem [8], [9]. The primary cause of data truncation arises from two scenarios: a)

The size of the imaged object exceeds the scanning field of view (FOV) due to the limited detector size [2]–[4], [10], [11]; b) In interior tomography, collimators are inserted to reduce unnecessary dose exposure for ROI imaging [12], [13].

Image reconstruction with the classic filtered back-projection (FBP) algorithm leads to cupping artifacts near the FOV boundary and missing (or severely distorted) anatomical structures outside the FOV boundary due to missing data [8]. Such degraded images could not fulfill clinical requirements. For example, adaptive radiotherapy based on truncated reconstruction images will lead inaccurate dose plannings [3]. To solve this problem, the most straightforward idea is to recover the missing data in the projection domain. Following this idea, heuristic data interpolation emerged. This method can estimate the missing projection data outside the FOV based on the existing mathematical model or the geometric prior knowledge of the object. Therefore, it can alleviate the cupping artifacts near the FOV boundary by smoothing the transition between the measured data and the truncated data. Among them are representative methods such as symmetrical mirror interpolation [14], geometric shape-based data estimation [15], and water cylinder extrapolation (WCE) [16]. With the rising of compressive sensing technology, iterative reconstruction algorithms with total variation regularization have been widely used to reconstruct images from insufficient projection data [9], such as sparse angle [17] and limited angle imaging [18] scenarios. For data truncation, minimizing the total variation loss can better reconstruct the images within the FOV [19], [20]. However, all the above-mentioned FOV extension algorithms, including extrapolation methods and compressed sensing methods both, can only improve the image quality within the FOV, but cannot restore the missing anatomical structures outside the FOV effectively [8].

In the recent decades, deep learning algorithms have achieved astonishing results in CT imaging tasks [21]–[23]. For CT FOV extension, researchers have proposed various deep learning methods, which can generally be classified into image domain, projection domain, and dual-domain. a) Image domain: Khural et al. [11] applied the U-Net network to expand the visual field of the image after linear interpolation and improved the image quality. b) Projection domain: Fonseca [2] proposed a visual field expansion algorithm called HDeep-FoV, which estimates the missing data outside the visual field through the FBPCnvNet network and then combines the results with the measurement data in the projection domain to reconstruct the final image. Huang et al. [8] proposed a Plug-and-Play framework, which improves the robustness and interpretability of the deep learning model by integrating measurement data consistency and the prior image information

This work involved human subjects or animals in its research. The authors confirm that all human/animal subject research procedures and protocols are exempt from review board approval (since only X-ray imaging data of human subjects from public data repository or other research projects were reused in this work).

Z. Li, L. Yang, X. Yin, J. Wang and W. Hu. are with Shanghai Cancer Center, Fudan University, Shanghai, China. H. Yu, H. Han and Y. Huang are with Institute of Medical Technology, Peking University Health Science Center, Beijing, China. Correspondence: huangyx@pku.edu.cn (Y.H.)

learned by the network. Tang et al. [24] adopted a similar idea and proposed Prior-FovNet, which uses the prior information of mega-voltage CT to expand the FOV of CBCT images. c) Dual-domain consistency: Gao et al. [3] proposed a dual-domain visual field expansion algorithm based on transformer, which restores the missing anatomical structures outside the visual field by considering the consistency of the image domain and the projection domain.

Diffusion models [25]–[28] are an emerging class of image generation models that degrade the image to a fully Gaussian noise by forward noise addition and obtain a high-quality target image conforming to the conditional distribution by sampling from known prior conditions through an inverse denoising process. The diffusion model has been widely used in image generation tasks due to its high image generation quality and stable training process, and has performed well for CT image reconstruction from insufficient data [29]–[31]. Nevertheless, the application of generative diffusion models to CT FOV extension has not been fully explored. Xie et al. [32] proposed a null space shuttle algorithm based on score-based generative model, which decomposes a CT image with limited FOV into zero space and range space, and gradually recovers the missing anatomical structures in the zero space by using diffusion model guided by a prior information in the range space. Nevertheless, the FOV is extended by a new trajectory scan, whereas the diffusion model is applied to improve image quality inside the scan FOV. Liman et al. [6] proposed an image extrapolation method based on the conditional diffusion model Palette [33], which recovers missing anatomical structures outside the scan FOV for body composition analysis. These studies demonstrate the powerful generative capacity of diffusion models.

Score-based generative models (SGMs) have demonstrated impressive sample quality and stable training performance in various image synthesis tasks [34], [35]. However, these models typically rely on a computationally intensive sampling process, requiring numerous iterative steps to progressively denoise Gaussian noise into realistic images. This slow sampling speed poses a major limitation for time-sensitive clinical applications [36]. Recently, substantial efforts have been made to reduce the computational cost of training and inference in diffusion models. For instance, the conditional latent diffusion model (cLDM) [29], [37] and the patch-based diffusion model (patchDiffusion) [38] enable efficient training with large-size images. The diffusion generative adversarial network (diffusionGAN) [39] enhances inference efficiency by adopting large sampling time steps using a multimodal Gaussian noise distribution. An emerging alternative is diffusion modeling based on the Schrödinger bridge (SB) [40]–[44], which enables direct transformation between two data distributions without the need to sample from a known noise prior. This framework naturally aligns with image-to-image translation tasks and offers a more efficient generative mechanism. In this study, we explore the application of a Schrödinger bridge diffusion model, known as Image-to-Image Schrödinger Bridge (I²SB) [43], to the task of CT FOV extension. Unlike conventional diffusion methods that start from Gaussian noise, I²SB directly learns the nonlinear stochastic process that maps limited-FOV

image distributions to extended-FOV image distributions. This direct modeling leads to improved sampling efficiency and image fidelity. By reducing the number of required sampling steps while maintaining high generation quality, I²SB offers a clinically practical solution for synthesizing extended-FOV CT images with enhanced stability and accuracy.

II. MATERIALS AND METHODS

A. Problem Formulation

Generally speaking, all CT reconstruction tasks can be regarded as a process of solving an inverse problem. Here, we use $\mathbf{x} \in \mathbb{R}^m$ to represent the original image data and $\mathbf{y} \in \mathbb{R}^n$ to represent the measurement data. In an ideal scenario, the measurement data \mathbf{y} can be expressed in terms of \mathbf{x} using the following formula:

$$\mathbf{y} = \mathbf{A}\mathbf{x}, \quad (1)$$

where $\mathbf{A} \in \mathbb{R}^{m \times n}$ denotes the system matrix, which serves to project the image data \mathbf{x} into the measurement data \mathbf{y} . With data truncation, solving Eqn. (1) becomes a severely ill-posed inverse problem, and conventional analytic and iterative algorithms fail to reconstruct structures outside the scan FOV precisely. This implies that more prior knowledge about the scanned object is needed to assist the reconstruction process. Deep learning methods have more capacity in this regard using data-driven learning than conventional analytic or iterative reconstruction algorithms. A direct idea to solve the data truncation problem is using a deep learning model with learnable parameter θ to establish the mapping from a limited FOV image \mathbf{x}_s to a normal FOV (or FOV-extended) image \mathbf{x}_l , which can be expressed as:

$$\mathbf{x}_l = f(\mathbf{x}_s; \theta) \quad (2)$$

Therefore, we can regard the task of restoring an image with limited FOV to an extended FOV image as an image-to-image generation task. In this work, we employ the I²SB method [43] to accomplish this task. Moreover, the WCE reconstruction is used as \mathbf{x}_s to reduce cupping artifacts and preliminarily restore some anatomical structures, which has been demonstrated to be more effective than a naive FBP reconstruction in our previous work [8].

B. Preliminaries in Diffusion Models

SGMs [34], [35] are a class of powerful generative frameworks that model data distributions via stochastic differential equations (SDEs). Given a sample \mathbf{x}_0 from a known data distribution $p(\mathbf{x}_0)$, SGMs define a forward diffusion process that gradually corrupts the data with noise, and a reverse process that restores it.

In the forward process, noise is progressively added to a clean image \mathbf{x}_0 until it becomes pure Gaussian noise. This process is governed by the following SDE:

$$d\mathbf{x}_t = \mathbf{f}_t(\mathbf{x}_t)dt + \sqrt{\beta_t}d\mathbf{w}_t, \quad (3)$$

where \mathbf{w}_t is a standard Wiener process, \mathbf{f}_t is the drift coefficient, and β_t is the diffusion coefficient, all potentially time-dependent. The time variable t typically ranges from 0 to

1 and is discretized into T steps. At $t = 0$, x_0 is the original data sample; at $t = 1$, the corrupted sample x_1 approximates a standard Gaussian distribution $\mathcal{N}(0, I)$.

To generate new data, SGMs define a reverse SDE that undoes this diffusion process:

$$dx_t = [f_t - \beta_t \nabla \log p(x_t, t)]dt + \sqrt{\beta_t}d\bar{w}_t \quad (4)$$

where $p(x_t, t)$ is the marginal distribution at time t , $\nabla \log p(x_t, t)$ is its score function (i.e., the gradient of the log-probability), and \bar{w}_t is a standard Wiener process running backward in time. Given an initial Gaussian noise sample x_1 and the score function at each time step, the clean image x_0 can be recovered by integrating this reverse SDE.

To estimate the score function $\nabla \log p(x_t, t)$, a denoising neural network ϵ_θ is trained using a scaled score matching objective:

$$\|\epsilon(x_t, t; \theta) - \sigma_t \nabla \log p(x_t, t|x_0)\|, \quad (5)$$

where σ_t denotes the standard deviation of the conditional distribution $p(x_t|x_0)$, which is typically known or analytically tractable. Once training converges, the model can perform posterior sampling using the following recursive relation:

$$x_t \sim p(x_t|\hat{x}_0, x_{t+1}), \quad x_T \sim \mathcal{N}(0, I), \quad (6)$$

where the estimated clean image \hat{x}_0 is computed from x_t and the network output as:

$$\hat{x}_0 := \frac{x_t - b_t \epsilon_\theta(x_t, t)}{a_t}, \quad (7)$$

based on the known formulation of the forward process, where a_t and b_t are process-specific coefficients. By recursively denoising through this reverse process, the model progressively reconstructs a clean image from Gaussian noise.

C. Image-to-Image Schrödinger Bridge

An SB [40] is a probabilistic model that formulates optimal transport between two distributions under entropy regularization. It defines a pair of forward and backward SDEs that evolve between two boundary distributions. The dynamics of the SB are given by:

$$dx_t = [f_t + \beta_t \nabla \log \Psi(x_t, t)]dt + \sqrt{\beta_t}dw_t, \quad (8)$$

$$dx_t = [f_t - \beta_t \nabla \log \hat{\Psi}(x_t, t)]dt + \sqrt{\beta_t}d\bar{w}_t, \quad (9)$$

where x_0 represents the normal FOV CT image sampled from the target distribution p_l , while x_1 represents the corresponding limited FOV CT image sampled from the source distribution p_s . The functions Ψ and $\hat{\Psi}$ represent time-dependent energy potentials that guide the transport process. These potentials satisfy the following coupled partial differential equations (PDEs):

$$\begin{cases} \frac{\partial \Psi(x, t)}{\partial t} = -\nabla \Psi^\top f - \frac{1}{2}\beta \nabla^2 \Psi, \\ \frac{\partial \hat{\Psi}(x, t)}{\partial t} = -\nabla \cdot (\hat{\Psi} f) + \frac{1}{2}\beta \nabla^2 \hat{\Psi}, \end{cases} \quad (10)$$

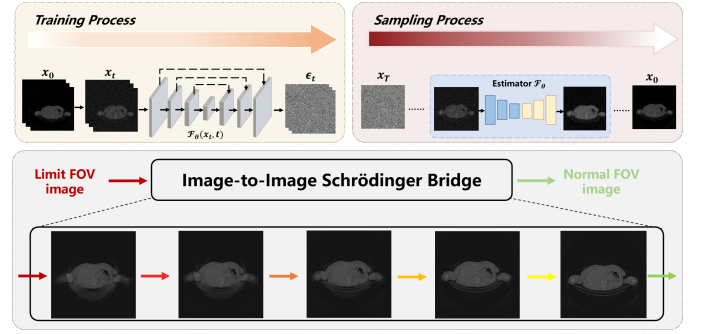


Fig. 1. The key difference in the image generation process between a conventional diffusion model and the image-to-image Schrödinger Bridge (I²SB) model is that the former begins from a noise image, while I²SB directly transforms an input image from one domain into its target counterpart. In this work, the limited FOV image is reconstructed by the water cylinder extrapolation (WCE) method [8].

These two potentials Ψ and $\hat{\Psi}$ are connected through the Nelson's duality [45]:

$$\Psi(x, t)\hat{\Psi}(x, t) = q(x, t), \quad (11)$$

where $q(x, t)$ denotes the evolving intermediate density, equivalent to $p(x, t)$ as used in the score-based diffusion formulation (see Eqn. (4)). As the SB framework seeks the most likely stochastic path connecting the two marginals p_l and p_s , the following boundary constraints are imposed:

$$\Psi(x, 0)\hat{\Psi}(x, 0) = p_l(x), \quad \Psi(x, 1)\hat{\Psi}(x, 1) = p_s(x). \quad (12)$$

Reformulating SB drifts as score functions, the nonlinear SDEs in Eqns. (10) are simplified to the following linear SDEs [43]:

$$dx_t = f_t(x_t)dt + \sqrt{\beta_t}dw_t, \quad x_0 \sim \hat{\Psi}(\cdot, 0) \quad (13)$$

$$dx_t = f_t(x_t)dt + \sqrt{\beta_t}d\bar{w}_t, \quad x_1 \sim \Psi(\cdot, 1) \quad (14)$$

The above equation makes the SB model compatible with the SGM, and $\nabla \hat{\Psi}(x_t, t)$ and $\nabla \log \Psi(x_t, t)$ are the score functions of the SDEs. Since Eqn. (12) establishes a two-way coupling between $\hat{\Psi}(\cdot, 0)$ and $\Psi(\cdot, T)$, this means that when solving for $\hat{\Psi}(\cdot, 0)$, $\Psi(\cdot, T)$ must also be taken into account simultaneously, complicating the problem-solving process. Therefore, according to [43], $\hat{\Psi}_0(\cdot)$ is assumed to be a Dirac δ distribution centered on each normal FOV CT image. With such an assumption, the initial distribution of the equation is given as:

$$\hat{\Psi}(\cdot, 0) = \delta_l(\cdot), \quad \Psi(\cdot, 1) = \frac{p_s}{\hat{\Psi}(\cdot, 1)}. \quad (15)$$

The above assumption breaks the dependency of $\hat{\Psi}(\cdot, 0)$ on $\Psi(\cdot, T)$, which enables us to directly establish a diffusion bridge between the two distributions without having to fix the starting point of the diffusion as Gaussian noise. The differences between I²SB and a conventional diffusion model architecture are shown in Fig. 1.

The specific process of applying the I²SB model to the CT FOV extension task is introduced in the following. x_0 represents an image with an extended FOV, while x_1 represents the corresponding image with a limit FOV. Any x_t that

drifts between \mathbf{x}_0 and \mathbf{x}_1 is designed to follow a Gaussian distribution $q(\mathbf{x}_t|\mathbf{x}_0, \mathbf{x}_1)$, which can be expressed as

$$q(\mathbf{x}_t|\mathbf{x}_0, \mathbf{x}_1) = \mathcal{N}(\mathbf{x}_t; \boldsymbol{\mu}_t(\mathbf{x}_0, \mathbf{x}_1), \boldsymbol{\Sigma}_t), \quad (16)$$

$$\boldsymbol{\mu}_t = \frac{\bar{\sigma}_t^2}{\bar{\sigma}_t^2 + \sigma_t^2} \mathbf{x}_0 + \frac{\sigma_t^2}{\bar{\sigma}_t^2 + \sigma_t^2} \mathbf{x}_1, \quad \boldsymbol{\Sigma}_t = \frac{\bar{\sigma}_t^2 \sigma_t^2}{\bar{\sigma}_t^2 + \sigma_t^2} \cdot \mathbf{I}, \quad (17)$$

where $\sigma_t^2 := \int_0^t \beta_\tau d\tau$ and $\bar{\sigma}_t^2 := \int_t^1 \beta_\tau d\tau$ are the variances accumulated in the interval $[0, 1]$ from either direction, respectively, and β_τ can determine the speed (or sampling step size) of the diffusion process. Since \mathbf{x}_t can be obtained at any time-steps using the equation above, the denoising network can be trained by a simple loss function,

$$\|\epsilon(\mathbf{x}_t, t; \boldsymbol{\theta}) - \frac{\mathbf{x}_t - \mathbf{x}_0}{\sigma_t}\|. \quad (18)$$

Therefore, the mapping model $\boldsymbol{\theta}$ from a limit FOV CT image to a normal FOV image becomes a simple parameterized noise estimator \mathcal{F}_θ . Once the noise estimator can precisely predict noise level in any timestep, it can be used to help the iterative reconstruction process and the details are as follows.

At any time step k in the reverse process, e.g. from \mathbf{x}_k to \mathbf{x}_{k-1} , $\hat{\mathbf{x}}_0$ can be calculated by the iterative last point \mathbf{x}_k and the estimated noise ϵ_θ ,

$$\hat{\mathbf{x}}_0^k = \mathbf{x}_k - \sigma_k \epsilon_\theta(\mathbf{x}_k, k). \quad (19)$$

Once $\hat{\mathbf{x}}_0^k$ is acquired, \mathbf{x}_{k-1} can be sampled from the posterior distribution $p(\mathbf{x}_{k-1}|\hat{\mathbf{x}}_0^k, \mathbf{x}_k)$, which can be expressed as:

$$p(\mathbf{x}_{k-1}|\hat{\mathbf{x}}_0^k, \mathbf{x}_k) = \mathcal{N}(\mathbf{x}_{k-1}; \frac{\alpha_{k-1}^2}{\sigma_k^2} \hat{\mathbf{x}}_0^k + \frac{\sigma_{k-1}^2}{\sigma_k^2} \mathbf{x}_k, \frac{\sigma_{k-1}^2 \alpha_{k-1}^2}{\sigma_k^2} \mathbf{I}), \quad (20)$$

where $\alpha_{k-1}^2 = \int_{k-1}^k \beta_\kappa d\kappa$ implies the accumulated variance between the timestep $k-1$ to k . After repeating the sampling process T times, we can obtain the final reconstructed image. However, the sampling process that involves T sampling steps takes a long time to complete. We can adjust the number of steps for evaluating the number of neural functions (NFE) to balance the computational efficiency and the quality of the reconstructed image. The advantage of I²SB is that NFE can be set to 1, which achieves high image generation efficiency without significant degradation of image quality.

D. Experiment Setup

1) *Simulated data*: The proposed I²SB algorithm for CT FOV extension was evaluated on simulated noisy data. The SMIR dataset [46] containing head and neck CT data from 53 patients was used for these experiments. Since this is a public open access data repository, informed consent was not required for researchers to reuse this dataset for research purpose. A Siemens Artis zee angiographic C-arm system was simulated to generate CBCT projections. The system parameters are displayed in Table I. Poisson noise was simulated assuming an incident photon number of 10^5 (i.e., $I_0 = 10^5$) for each detector pixel. The 3D Feldkamp-Davis-Kress (FDK) reconstruction with WCE [16] was used to compute the reconstruction from

TABLE I
PARAMETERS FOR SIMULATING IMAGING SYSTEM IN EXPERIMENTS.

Parameters	Values
Source-to-detector distance d_1 (mm)	900
Source-to-isocenter distance d_2 (mm)	600
Size of detector (pixels)	1240×960
Pixels size (mm)	1.0
FOV diameter (cm)	34
Reconstruction volume size (voxels)	$512 \times 512 \times 512$
Voxel size (mm)	$1.27 \times 1.27 \times 1.27$

truncated projection data. The reconstructed volumes have a size of $512 \times 512 \times 512$ with a voxel size of $1.27 \text{ mm} \times 1.27 \text{ mm} \times 1.27 \text{ mm}$. The original scan FOV diameter is 34 cm. The extended FOV images have a diameter of 65 cm. For each volume, one slice among every 10 axial slices was chosen for training, validation, or testing. 2050 slices from 41 patients were used for training, 50 slices from one patient was used for validation, and 500 slices from 10 patients were used for testing. As a proof-of-concept study, 512×512 images were rebinned to 256×256 images to save computational resources and experimental time.

2) *Real data*: To better verify the usability of the proposed algorithm, an evaluation on a 3D clinical head dataset with a typical noise level was conducted as well. The head dataset was collected using the Artis zee vascular angiography C-arm system (Siemens Healthcare GmbH, Forchheim). Since this data has been scanned for prior projects [8], ethical review and approval was not required for this study in accordance with the local legislation and institutional requirements (BayKrG Art. 27). The dose area product (DAP) of the entire scan was $532 \mu\text{Gy} \cdot \text{m}^2$. The detector size was 1240×960 pixels, and the detector pixel size was $0.308 \text{ mm} \times 0.308 \text{ mm}$. The entire dataset contained 496 projections obtained from a 200° short scan. The reconstructed volume size was $512 \times 512 \times 300$ With an isotropic voxel size of $0.465 \text{ mm} \times 0.465 \text{ mm} \times 0.465 \text{ mm}$. For ROI imaging, the central 600×960 pixels of the projection data were used, while the other pixels were collimated. The FOV diameter was reduced from 23.9 cm to 11.6 cm because of the collimation.

In this study, we selected 2880 slices from the CQ500 head CT data collection [47] to simulate WCE reconstruction and full reconstruction image pairs in the same C-arm system as the real data to train the model. To achieve a similar noise level, Poisson noise was added to the input training slices, considering the exposure before attenuation for each detector pixel to be $I_0 = 5 \times 10^5$ photons.

3) *Network parameters*: All the experiments were conducted on a GPU server with GeForce A6000 GPUs. The WCE images were used as the input images of the learning-based methods, which have advantages over FBP images as the input as found in our previous study [8]. For the proposed I²SB algorithm, we followed to set a symmetric scheduling β_t , the total time-steps $K = 1000$ and initialized the network with the unconditional ADM checkpoint [27] trained on ImageNet 256×256 .

Followed by [43], the maximum of hyperparameter β_t was set to 0.3. The model was trained and tested at a size of 256

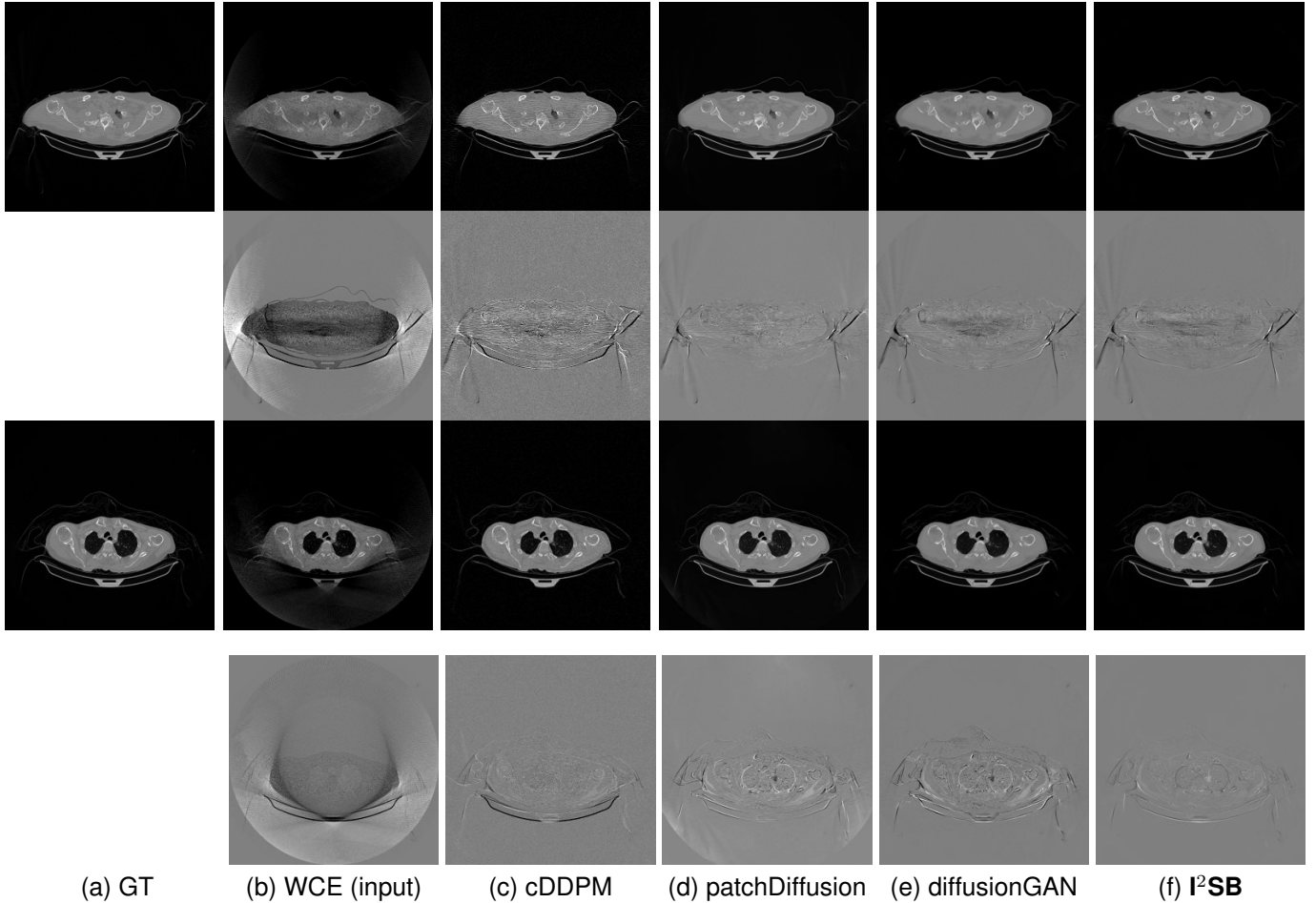


Fig. 2. Results of two exemplary test slices in the noisy scenario. The first and third rows represent different slices in the test set, and the second and fourth rows show the error maps. The display window is $[-1000, 1000]$ HU for the reconstruction images and $[-500, 500]$ HU for the error maps.

$\times 256$ images. A batch size of 32 and a micro batch size of 4 were employed during training, using the Adam optimizer with a learning rate of 5×10^{-5} for 200,000 iterations.

4) *Comparison models*: To verify the performance of the proposed I^2SB algorithm, we compared it with several prominent image-to-image translation algorithms such as the FBP-ConvNet [48], Pix2pixGAN [49], the conditional denoising diffusion probabilistic model (cDDPM) [50], cLDM [29], [37], patchDiffusion [38], and diffusionGAN [39]. To ensure network convergence, the number of training epochs for FBP-ConvNet and Pix2pixGAN was set to 200. While cDDPM and patchDiffusion are based on the original DDPM architecture, the condition images in these models were added by concatenate on channel dimension, and their training iterations were set to 1×10^6 . For cLDM, its variational autoencoder (VAE) was first fine-tuned on the target dataset and then trained for 1000 epochs.

This article used three common objective image evaluation parameters, including root mean square error (RMSE), peak signal-to-noise ratio (PSNR), and structural similarity index (SSIM), to evaluate image quality.

III. RESULTS

A. Results of Simulated Noisy Data

The results for simulated noisy data are shown in Fig. 2. The first and third rows display two representative slices from the test set, and the second and fourth rows present the corresponding error maps. The traditional WCE method suppresses cupping artifacts and recovers some missing anatomical structures but still shows noticeable deviations from the ground truth. Predictions from the four diffusion-based models demonstrate a markedly improved ability to restore anatomical structures. Among them, cDDPM fails to fully reconstruct the patient bed and retains residual noise in its outputs. This noise is attributable to an incomplete reverse denoising process rather than residual Poisson noise, as evidenced in our noise-free experiments (Fig. 5 in the Appendix). PatchDiffusion, diffusionGAN, and I^2SB achieve similar visual quality, with I^2SB producing the cleanest and most consistent reconstructions.

Quantitative results in Tab. V further confirm I^2SB 's superiority over conventional deep learning methods such as FBPConvNet and Pix2pixGAN across RMSE, PSNR, and SSIM. Compared to other diffusion models—including cDDPM, PatchDiffusion, and cLDM— I^2SB delivers higher image quality, while diffusionGAN achieves comparable quanti-

tative performance. However, I^2SB demonstrates a significant advantage in inference efficiency, as summarized in Tab. IV.

TABLE II
QUANTITATIVE COMPARISON IN THE NOISY SCENARIO.

Methods	RMSE	PSNR	SSIM
FBP	288.6	20.17	0.3103
WCE	168.4	22.29	0.5236
Pix2pixGAN	110.8	25.45	0.7611
FBPConvNet	60.8	30.43	0.8793
cDDPM	76.8	34.84	0.8475
cLDM	60.8	30.66	0.8846
patchDiffusion	65.2	30.11	0.5636
diffusionGAN	48.0	38.91	0.9527
I^2SB (proposed)	49.8	38.75	0.9473

B. Efficiency Analysis

We further conducted reconstructions using the model with different number of NFEs. Here, in order to enhance the assessment efficiency, the number of test images was set to 250. The statistical results of the evaluation metrics are presented in Table III. From the perspective of statistical parameters, the difference in the number of NFEs has only a minor impact on image quality. However, as the number of function evaluations increases, the sampling time for each image rapidly rises, reducing the reconstruction efficiency. Therefore, one-step generation can be regarded as the optimal number of NFEs in this task.

The inference times per 2D slice for different methods are summarized in Tab. IV. FBPConvNet and Pix2pixGAN, which require no iterative sampling, achieve inference times below 0.5 s. In contrast, the cDDPM model takes over 2 minutes due to its reliance on hundreds of reverse sampling steps. The patchDiffusion model shortens this to 6.2 s, while diffusionGAN, with only four reverse sampling steps, achieves 0.57 s. Benefiting from a single-step sampling process, I^2SB attains the fastest inference time among all diffusion-based methods, at just 0.19 s.

C. Uncertainty analysis

Classical diffusion models reconstruct images by progressively denoising from an initial Gaussian noise image, a process that inherently introduces uncertainty due to random noise initialization. In contrast, I^2SB directly learns a diffusion bridge between two sample distributions, effectively bypassing the need for random noise sampling and thereby reducing reconstruction variability.

To assess the uncertainty of our method, we performed multiple reconstructions using different random seeds. As shown in Fig. 3, the ground truth and representative sampled images are presented in Fig. 3(a) and (b–d), respectively. The mean reconstruction and pixel-wise standard deviation across runs are displayed in Fig. 3(e) and (f). Only minimal differences are observed between reconstructions, indicating that I^2SB produces highly consistent results. These findings confirm that, compared with classical diffusion models, I^2SB substantially reduces uncertainty across repeated reconstructions.

TABLE III
THE INFLUENCE OF NFE ON IMAGE QUALITY.

NFE	RMSE	PSNR	SSIM
1	49.8	38.74	0.9473
5	50.6	38.66	0.9475
10	50.4	38.69	0.9475
25	50.6	38.66	0.9467

TABLE IV
INFERENCE TIME COMPARISON USING DIFFERENT METHODS

Method	Time (s)
FBPConvNet	0.22
Pix2pixGAN	0.43
cDDPM	135.46
patchDiffusion	6.24
diffusionGAN	0.57
I^2SB	0.19

D. Real Clinical Data Experiment

The experimental results on clinical head data are shown in Fig. 4. The reference images were reconstructed using the fast iterative shrinkage-thresholding algorithm (FISTA) with total variation regularization from non-truncated projection data. In the WCE reconstructions (Fig. 4(b)), severe truncation prevents accurate recovery of anatomical structures outside the FOV. Despite being trained solely on simulated data with a domain gap, all deep learning models can restore a substantial portion of the missing anatomy. Among them, the diffusion-based methods recover soft-tissue boundaries more faithfully than the conventional deep learning approach FBPConvNet, highlighting their stronger image generation capability. However, cDDPM reconstructions exhibit more noticeable noise than those from other methods, consistent with the simulated data results. The patchDiffusion model introduces artifacts within the FOV, likely due to its patch-wise processing strategy. While I^2SB shares the same limitations as other diffusion models in perfectly restoring soft-tissue detail, it produces fewer residual noise patterns and fewer artifacts within the FOV boundaries. Overall, Fig. 4 demonstrates the strong efficacy of I^2SB in reconstructing real CBCT data.

TABLE V
QUANTITATIVE COMPARISON IN THE NOISY SCENARIO.

Methods	RMSE	PSNR	SSIM
FBP	425.3	19.68	0.4372
WCE	382.2	21.16	0.6642
Pix2pixGAN	279.8	23.41	0.5702
FBPConvNet	260.0	24.19	0.6181
cDDPM	190.2	26.94	0.6482
patchDiffusion	231.8	25.25	0.6839
diffusionGAN	162.1	28.19	0.6798
I^2SB (proposed)	152.0	28.72	0.7260

IV. DISCUSSION

In this work, we investigated several diffusion models for the task of CT FOV extension, formulated as an image-to-image translation problem. Conventional diffusion models

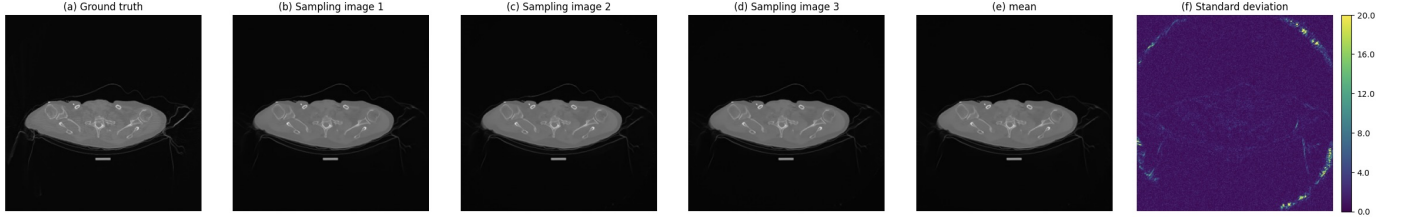


Fig. 3. Quantifying the uncertainty of reconstruction. (a) Ground truth, (b-d) sampling images with different random seed, (e) mean of the reconstruction, (f) standard deviation of the samples: range is set to [0, 20] (on Viridis colormap).

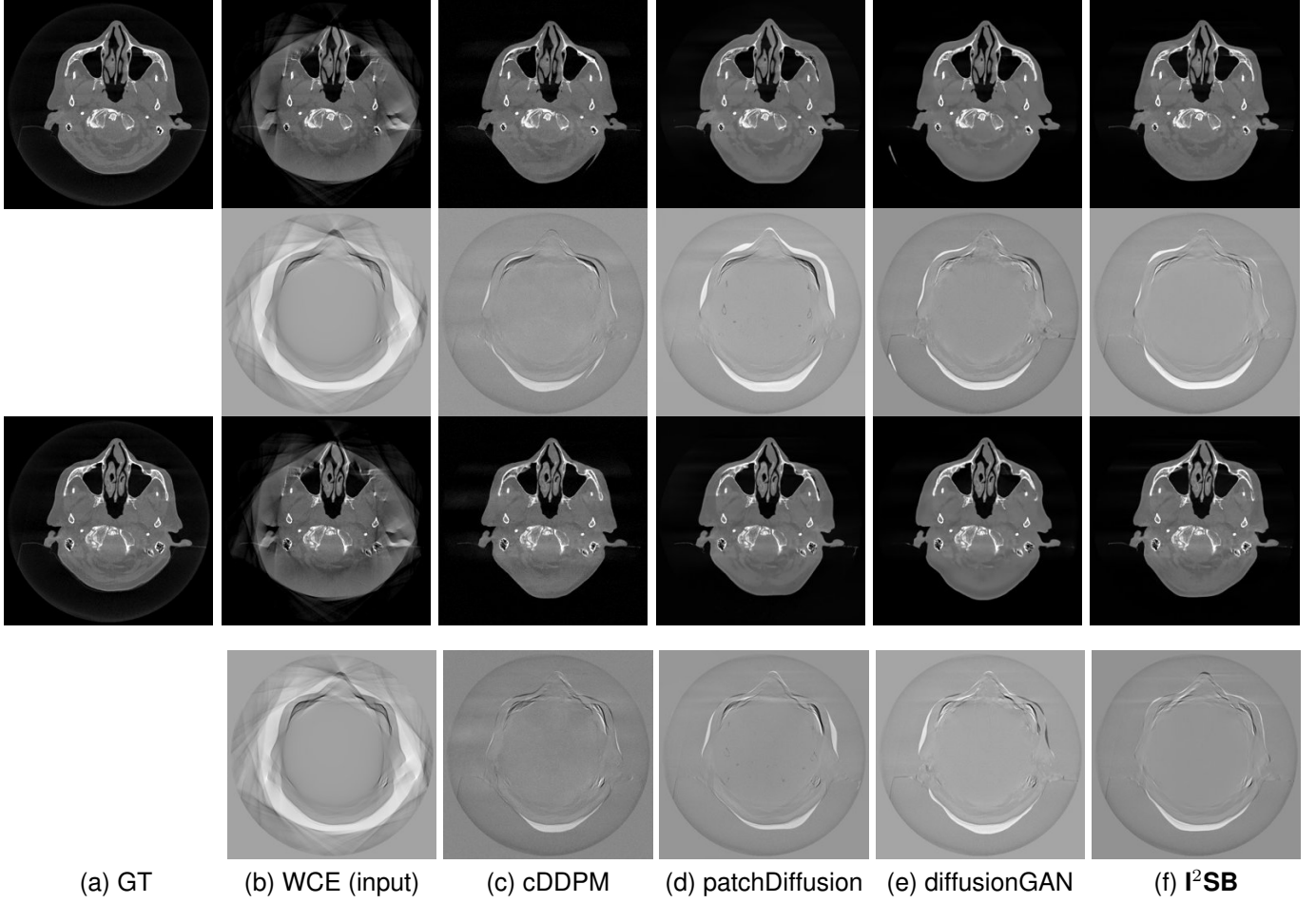


Fig. 4. Results of two exemplary test slices in the real data. The first and third rows represent different slices in the test set, and the second and fourth rows show the error maps. The display window is [-1000, 1000] HU for the reconstruction images and the error maps.

have demonstrated strong performance in image generation, but their practical application is constrained by long inference times and high training costs. The proposed I²SB model addresses these limitations by directly establishing a diffusion bridge between the limited-FOV and extended-FOV images. Unlike classical diffusion models, I²SB does not require transforming the image into pure Gaussian noise; instead, inference begins from the truncated image itself. This approach reduces the number of sampling steps required while better preserving anatomical structure consistency. Our results show that, even with a single sampling step, I²SB outperforms traditional reconstruction methods such as Pix2pixGAN and FBPCNet, as well as other diffusion models including cDDPM and PatchDiffusion. We attribute this advantage to the

direct mapping between the two distributions, which mitigates information loss from noise-based initialization and avoids the uncertainty introduced during stochastic sampling in classical diffusion models.

Owing to its one-step inference, I²SB achieves exceptional computational efficiency, reconstructing a slice in just 0.19 s. Compared with cDDPM (135 s per slice), this represents more than a 700-fold speedup (Tab. IV). This acceleration is achieved without compromising reconstruction quality, thereby improving the accessibility of extended-FOV images and enhancing their applicability in downstream clinical and research tasks. Among other diffusion models, diffusionGAN also achieves rapid inference (0.57 s per slice) by using large sampling time steps and delivers comparable image quality.

However, the diffusion GAN still requires adversarial training, which makes its training process less stable compared to I^2SB .

We validated I^2SB and other diffusion models on both simulated noisy data and real head CBCT data. For the real data, the most prominent errors occurred in the soft tissues near the head boundary. This is primarily because the WCE method assumes that missing projection data corresponds to soft-tissue (water-equivalent) attenuation, making it challenging for deep learning models to accurately estimate the true boundary. In addition, the training data were simulated from the CQ500 dataset using the same C-arm CBCT system, introducing an inevitable domain gap between simulated training data and real test data. Future work will focus on acquiring more real CBCT data to train I^2SB , which is expected to further improve reconstruction quality and generalization performance.

V. CONCLUSION

In this work, we proposed an efficient and interpretable CT FOV extension algorithm based on the I^2SB diffusion model. By directly learning a mapping between limited-FOV and extended-FOV CT images, I^2SB addresses the limitations of traditional diffusion models that rely on time-consuming, noise-based sampling. Our model offers a clear generative path from input to output, preserving anatomical consistency while improving the traceability of the reconstruction process. Extensive experiments conducted on both simulated noisy data and real data demonstrate that I^2SB outperforms existing state-of-the-art methods, including cDDPM and patchDiffusion, in terms of image quality and inference efficiency. Its fast inference time of 0.19 s per 2D slice makes it highly suitable for time-sensitive clinical applications. Overall, I^2SB provides a promising solution for FOV extension in CT imaging by combining the strengths of diffusion models with the efficiency and practicality required for real-world deployment.

ACKNOWLEDGMENTS

The authors declare that they have no known competing financial interests or personal relationships that could have appeared to influence the work reported in this paper.

REFERENCES

- [1] L. Yang, X. Yin, Z. Li, Z. Ding, Y. Zou, Z. Li, E. Mo, Q. Zhou, J. Wang, and W. Hu, "Adaptive radiotherapy triggering for nasopharyngeal cancer based on bayesian decision model," *Physics in Medicine & Biology*, vol. 70, no. 7, p. 075015, 2025.
- [2] G. P. Fonseca, M. Baer-Beck, E. Fournie, C. Hofmann, I. Rinaldi, M. C. Ollers, W. J. van Elmpt, and F. Verhaegen, "Evaluation of novel AI-based extended field-of-view CT reconstructions," *Medical physics*, vol. 48, no. 7, pp. 3583–3594, 2021.
- [3] L. Gao, K. Xie, J. Sun, T. Lin, J. Sui, G. Yang, and X. Ni, "A transformer-based dual-domain network for reconstructing FOV extended cone-beam CT images from truncated sinograms in radiation therapy," *Computer methods and programs in biomedicine*, vol. 241, p. 107767, 2023.
- [4] F. Fan, B. Kreher, H. Keil, A. Maier, and Y. Huang, "Fiducial marker recovery and detection from severely truncated data in navigation-assisted spine surgery," *Medical Physics*, vol. 49, pp. 2914–2930, 2022.
- [5] K. Xu, T. Li, M. S. Khan, R. Gao, S. L. Antic, Y. Huo, K. L. Sandler, F. Maldonado, and B. A. Landman, "Body composition assessment with limited field-of-view computed tomography: A semantic image extension perspective," *Medical Image Analysis*, vol. 88, p. 102852, 2023.
- [6] M. E. Liman, D. Rueckert, F. J. Fintelmann, and P. Müller, "Diffusion-Based Generative Image Outpainting for Recovery of FOV-Truncated CT Images," in *International Conference on Medical Image Computing and Computer-Assisted Intervention*. Springer, 2024, pp. 14–23.
- [7] Y. Xia, H. Hofmann, F. Dennerlein, K. Mueller, C. Schwemmer, S. Bauer, G. Chintalapani, P. Chinnadurai, J. Horneberger, and A. Maier, "Towards clinical application of a laplace operator-based region of interest reconstruction algorithm in C-arm CT," *IEEE Trans. Med. Imaging*, vol. 33, no. 3, pp. 593–606, 2013.
- [8] Y. Huang, A. Preuhs, M. Manhart, G. Lauritsch, and A. Maier, "Data extrapolation from learned prior images for truncation correction in computed tomography," *IEEE Transactions on Medical Imaging*, vol. 40, no. 11, pp. 3042–3053, 2021.
- [9] T. Wang, W. Xia, J. Lu, and Y. Zhang, "A review of deep learning ct reconstruction from incomplete projection data," *IEEE Transactions on Radiation and Plasma Medical Sciences*, vol. 8, no. 2, pp. 138–152, 2023.
- [10] Y. Huang, L. Gao, A. Preuhs, and A. Maier, "Field of view extension in computed tomography using deep learning prior," in *Proc. BVM*, 2020, pp. 186–191.
- [11] B. S. Khural, M. Baer-Beck, E. Fournié, K. Stierstorfer, Y. Huang, and A. Maier, "Deep learning-based extended field of view computed tomography image reconstruction: influence of network design on image estimation outside the scan field of view," *Biomedical Physics & Engineering Express*, vol. 8, no. 2, p. 025021, 2022.
- [12] L. Yu, Y. Zou, E. Y. Sidky, C. A. Pelizzari, P. Munro, and X. Pan, "Region of interest reconstruction from truncated data in circular cone-beam CT," *IEEE Trans. Med. imaging*, vol. 25, pp. 869–881, 2006.
- [13] H. Yu, Y. Ye, and G. Wang, "Interior reconstruction using the truncated Hilbert transform via singular value decomposition," *Journal of X-ray science and technology*, vol. 16, no. 4, pp. 243–251, 2008.
- [14] B. Ohnesorge, T. Flohr, K. Schwarz, J. Heiken, and K. Bae, "Efficient correction for CT image artifacts caused by objects extending outside the scan field of view," *Medical physics*, vol. 27, no. 1, pp. 39–46, 2000.
- [15] T. Hu, B. Li, J. Yang, B. Zhang, L. Fang, Y. Liu, P. Xiao, and Q. Xie, "Application of geometric shape-based CT field-of-view extension algorithms in an all-digital positron emission tomography/computed tomography system," *Medical Physics*, vol. 51, no. 2, pp. 1034–1046, 2024.
- [16] J. Hsieh, E. Chao, J. Thibault, B. Grekowicz, A. Horst, S. McOlash, and T. Myers, "A novel reconstruction algorithm to extend the CT scan field-of-view," *Medical physics*, vol. 31, no. 9, pp. 2385–2391, 2004.
- [17] Y. Liu, Z. Liang, J. Ma, H. Lu, K. Wang, H. Zhang, and W. Moore, "Total Variation-Stokes Strategy for Sparse-View X-ray CT Image Reconstruction," *IEEE Transactions on Medical Imaging*, vol. 33, no. 3, pp. 749–763, 2014.
- [18] Y. Huang, O. Taubmann, X. Huang, V. Haase, G. Lauritsch, and A. Maier, "Scale-Space Anisotropic Total Variation for Limited Angle Tomography," *IEEE Transactions on Radiation and Plasma Medical Sciences*, vol. 2, no. 4, pp. 307–314, 2018.
- [19] H. Yu and G. Wang, "Compressed sensing based interior tomography," *Phys. Med. Biol.*, vol. 54, no. 9, p. 2791, 2009.
- [20] W. Han, H. Yu, and G. Wang, "A general total variation minimization theorem for compressed sensing based interior tomography," *Int. J. Biomed. Imaging*, vol. 2009, 2009.
- [21] Y. Huang, A. Maier, F. Fan, B. Kreher, X. Huang, R. Fietkau, H. Han, F. Putz, and C. Bert, "Learning Perspective Distortion Correction in Cone-Beam X-Ray Transmission Imaging," *IEEE Transactions on Radiation and Plasma Medical Sciences*, 2025.
- [22] Q. Gao, Z. Li, J. Zhang, Y. Zhang, and H. Shan, "CoreDiff: Contextual error-modulated generalized diffusion model for low-dose CT denoising and generalization," *IEEE Transactions on Medical Imaging*, vol. 43, no. 2, pp. 745–759, 2024.
- [23] Y. Xu, J. Wang, and W. Hu, "Prior-image-based low-dose CT reconstruction for adaptive radiation therapy," *Physics in Medicine & Biology*, vol. 69, no. 21, p. 215004, 2024.
- [24] L. Tang, M. Zheng, P. Liang, Z. Li, Y. Zhu, and H. Zhang, "Prior-FOVNet: A multimodal deep learning framework for megavoltage computed tomography truncation artifact correction and field-of-view extension," *Sensors*, vol. 25, no. 1, p. 39, 2024.
- [25] Y. Song, J. Sohl-Dickstein, D. P. Kingma, A. Kumar, S. Ermon, and B. Poole, "Score-based generative modeling through stochastic differential equations," in *International Conference on Learning Representations*, 2021, pp. 1–36.
- [26] J. Ho, A. Jain, and P. Abbeel, "Denoising diffusion probabilistic models," *Advances in neural information processing systems*, vol. 33, pp. 6840–6851, 2020.

- [27] P. Dhariwal and A. Nichol, “Diffusion models beat gans on image synthesis,” *Advances in neural information processing systems*, vol. 34, pp. 8780–8794, 2021.
- [28] A. Q. Nichol and P. Dhariwal, “Improved denoising diffusion probabilistic models,” in *International conference on machine learning*. PMLR, 2021, pp. 8162–8171.
- [29] L. Hou, J. Liu, X. Li, and Y. Sun, “Two-view industrial CT reconstruction based on a multi-scale conditional latent diffusion network,” *IEEE Transactions on Instrumentation and Measurement*, 2024.
- [30] J. Xie, H.-C. Shao, Y. Li, and Y. Zhang, “Prior frequency guided diffusion model for limited angle (LA)-CBCT reconstruction,” *Physics in Medicine & Biology*, vol. 69, no. 13, p. 135008, 2024.
- [31] J. Zhang, H. Mao, X. Wang, Y. Guo, and W. Wu, “Wavelet-inspired multi-channel score-based model for limited-angle CT reconstruction,” *IEEE Transactions on Medical Imaging*, vol. 43, no. 10, pp. 3436–3448, 2024.
- [32] H. Xie, H. Yu, S. Ni, C. Tan, G. Zhang, Z. Wang, M. Zhan, and F. Liu, “Score-based generative null-space shuttle for the field-of-view of STCT expansion,” *IEEE Transactions on Radiation and Plasma Medical Sciences*, vol. 9, no. 6, pp. 776–787, 2025.
- [33] C. Saharia, W. Chan, H. Chang, C. Lee, J. Ho, T. Salimans, D. Fleet, and M. Norouzi, “Palette: Image-to-image diffusion models,” in *ACM SIGGRAPH 2022 conference proceedings*, 2022, pp. 1–10.
- [34] L. Yang, Z. Zhang, Y. Song, S. Hong, R. Xu, Y. Zhao, W. Zhang, B. Cui, and M.-H. Yang, “Diffusion models: A comprehensive survey of methods and applications,” *ACM computing surveys*, vol. 56, no. 4, pp. 1–39, 2023.
- [35] F.-A. Croitoru, V. Hondru, R. T. Ionescu, and M. Shah, “Diffusion models in vision: A survey,” *IEEE transactions on pattern analysis and machine intelligence*, vol. 45, no. 9, pp. 10 850–10 869, 2023.
- [36] Z. Zhou, D. Chen, C. Wang, and C. Chen, “Fast ode-based sampling for diffusion models in around 5 steps,” in *Proceedings of the IEEE/CVF Conference on Computer Vision and Pattern Recognition*, 2024, pp. 7777–7786.
- [37] R. Rombach, A. Blattmann, D. Lorenz, P. Esser, and B. Ommer, “High-resolution image synthesis with latent diffusion models,” in *Proceedings of the IEEE/CVF conference on computer vision and pattern recognition*, 2022, pp. 10 684–10 695.
- [38] Z. Wang, Y. Jiang, H. Zheng, P. Wang, P. He, Z. Wang, W. Chen, M. Zhou *et al.*, “Patch diffusion: Faster and more data-efficient training of diffusion models,” *Advances in neural information processing systems*, vol. 36, pp. 72 137–72 154, 2023.
- [39] Z. Xiao, K. Kreis, and A. Vahdat, “Tackling the generative learning trilemma with denoising diffusion GANs,” in *International Conference on Learning Representations (ICLR)*, 2022, pp. 1–28.
- [40] E. Schrödinger, “Sur la théorie relativiste de l’électron et l’interprétation de la mécanique quantique,” in *Annales de l’institut Henri Poincaré*, vol. 2, no. 4, 1932, pp. 269–310.
- [41] V. De Bortoli, J. Thornton, J. Heng, and A. Doucet, “Diffusion schrödinger bridge with applications to score-based generative modeling,” *Advances in neural information processing systems*, vol. 34, pp. 17 695–17 709, 2021.
- [42] Y. Shi, V. De Bortoli, A. Campbell, and A. Doucet, “Diffusion schrödinger bridge matching,” *Advances in Neural Information Processing Systems*, vol. 36, pp. 62 183–62 223, 2023.
- [43] G.-H. Liu, A. Vahdat, D.-A. Huang, E. A. Theodorou, W. Nie, and A. Anandkumar, “I²SB: Image-to-image Schrödinger Bridge,” in *International Conference on Machine Learning*, 2023, pp. 1–21.
- [44] M. Li, X. Li, S. Safai, A. J. Lomax, and Y. Zhang, “Diffusion schrödinger bridge models for high-quality mr-to-ct synthesis for proton treatment planning,” *Medical Physics*, 2025.
- [45] E. NELSON, *Dynamical Theories of Brownian Motion*. Princeton University Press, 1967.
- [46] M. Kistler, S. Bonaretti, M. Pfahrer, R. Niklaus, and P. Büchler, “The virtual skeleton database: An open access repository for biomedical research and collaboration,” *J Med Internet Res*, vol. 15, no. 11, p. e245, Nov 2013.
- [47] S. Chilamkurthy, R. Ghosh, S. Tanamala, M. Biviji, N. G. Campeau, V. K. Venugopal, V. Mahajan, P. Rao, and P. Warier, “Deep learning algorithms for detection of critical findings in head ct scans: a retrospective study,” *The Lancet*, vol. 392, no. 10162, pp. 2388–2396, 2018.
- [48] K. H. Jin, M. T. McCann, E. Froustey, and M. Unser, “Deep convolutional neural network for inverse problems in imaging,” *IEEE Transactions on Image Processing*, vol. 26, no. 9, pp. 4509–4522, 2017.
- [49] P. Isola, J.-Y. Zhu, T. Zhou, and A. A. Efros, “Image-to-image translation with conditional adversarial networks,” in *Proceedings of the IEEE conference on computer vision and pattern recognition*, 2017, pp. 1125–1134.
- [50] J. Peng, R. L. Qiu, J. F. Wynne, C.-W. Chang, S. Pan, T. Wang, J. Roper, T. Liu, P. R. Patel, D. S. Yu *et al.*, “CBCT-Based synthetic CT image generation using conditional denoising diffusion probabilistic model,” *Medical physics*, vol. 51, no. 3, pp. 1847–1859, 2024.

VI. APPENDIX

A. Results of Noise-Free Data

The results of the noise-free experiments are shown in Fig. 5. It is worth noting that residual noise remains in the generated images despite the noise-free setting in the case of cDDPM, indicating incomplete denoising during the reverse diffusion process. Both patchDiffusion and I²SB achieve comparable, high-quality reconstructions and clearly outperform cDDPM, which is consistent with the results in the noisy data experiments (see Fig. 2). However, I²SB demonstrates better generalizability for real data (Fig. 4) and a significant advantage in inference efficiency (Tab. IV).

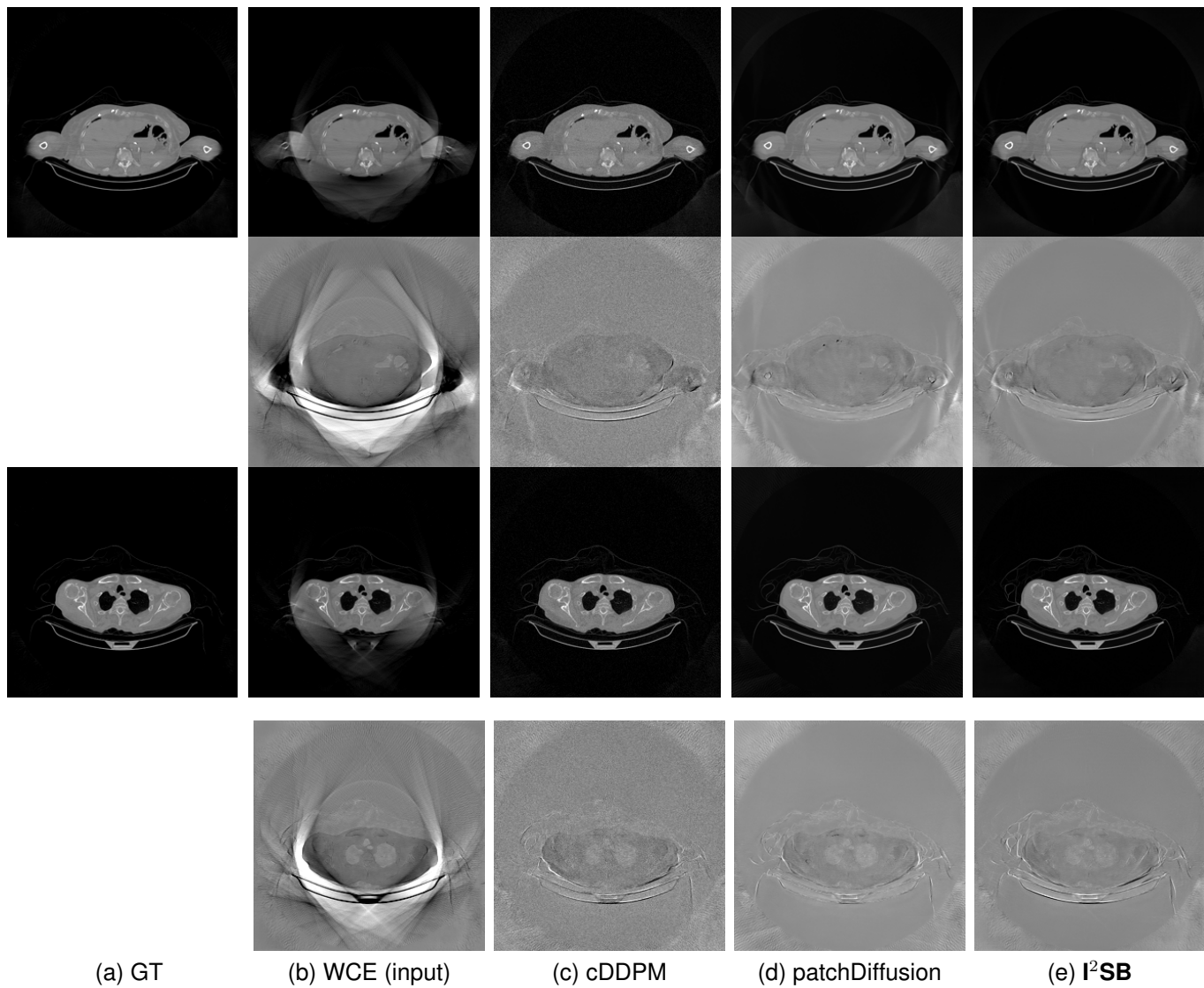


Fig. 5. Results of two exemplary test slices in the noise-free scenario. The first and third rows represent different slices in the test set, and the second and fourth rows show the error maps. The display window is $[-1000, 1000]$ HU for the reconstruction images and $[-500, 500]$ HU for the error maps.